Complete Methods Set for Scalable Ion Trap Quantum Information Processing
Jonathan P. Home, *et al.*
Science **325**, 1227 (2009);
DOI: 10.1126/science.1177077

a general tool to tailor interactions in 1D and possibly also in 2D systems (*28*), allowing for the further investigation of strongly correlated phases in the context of cold atomic gases.

References and Notes

1. M. Girardeau, *J. Math. Phys.* **1**, 516 (1960).
2. E. H. Lieb, W. Liniger, *Phys. Rev.* **130**, 1605 (1963).
3. B. Paredes *et al.*, *Nature* **429**, 277 (2004).
4. T. Kinoshita, T. Wenger, D. S. Weiss, *Science* **305**, 1125 (2004).
5. F. Alet, A. M. Walczak, M. P. A. Fisher, *Physica A* **369**, 122 (2006).
6. D. S. Petrov, G. V. Shlyapnikov, J. T. M. Walraven, *Phys. Rev. Lett.* **85**, 3745 (2000).
7. H. Moritz, T. Stöferle, M. Köhl, T. Esslinger, *Phys. Rev. Lett.* **91**, 250402 (2003).
8. B. L. Tolra *et al.*, *Phys. Rev. Lett.* **92**, 190401 (2004).
9. D. S. Petrov, D. M. Gangardt, G. V. Shlyapnikov, *J. Phys. IV France* **116**, 3 (2004).
10. S. Hofferberth, I. Lesanovsky, B. Fischer, T. Schumm, J. Schmiedmayer, *Nature* **449**, 324 (2007).
11. N. Syassen *et al.*, *Science* **320**, 1329 (2008).
12. I. Bloch, J. Dalibard, W. Zwerger, *Rev. Mod. Phys.* **80**, 885 (2008).
13. G. E. Astrakharchik, J. Boronat, J. Casulleras, S. Giorgini, *Phys. Rev. Lett.* **95**, 190407 (2005).
14. T. Bergeman, M. G. Moore, M. Olshanii, *Phys. Rev. Lett.* **91**, 163201 (2003).
15. M. Olshanii, *Phys. Rev. Lett.* **81**, 938 (1998).
16. C. Menotti, S. Stringari, *Phys. Rev. A* **66**, 043610 (2002).
17. S. Inouye *et al.*, *Nature* **392**, 151 (1998).
18. J. B. McGuire, *J. Math. Phys.* **6**, 432 (1965).
19. E. Tempfli, S. Zöllner, P. Schmelcher, *N.J. Phys.* **10**, 103021 (2008).
20. M. T. Batchelor, M. Bortz, X. W. Guan, N. Oelkers, *J. Stat. Mech.* **10**, L10001 (2005).
21. G. E. Astrakharchik, D. Blume, S. Giorgini, B. E. Granger, *Phys. Rev. Lett.* **92**, 030402 (2004).
22. T. Weber, J. Herbig, M. Mark, H.-C. Nägerl, R. Grimm, *Science* **299**, 232 (2003).
23. A. D. Lange *et al.*, *Phys. Rev. A* **79**, 013622 (2009).
24. Material and methods are available as supporting material on *Science* Online.
25. T. Kinoshita, T. Wenger, D. S. Weiss, *Nature* **440**, 900 (2006).
26. M. Bockrath *et al.*, *Nature* **397**, 598 (1999).
27. H. Steinberg *et al.*, *Nat. Phys.* **4**, 116 (2008).
28. D. S. Petrov, M. Holzmann, G. V. Shlyapnikov, *Phys. Rev. Lett.* **84**, 2551 (2000).

Complete Methods Set for Scalable Ion Trap Quantum Information Processing

Jonathan P. Home,* David Hanneke, John D. Jost, Jason M. Amini, Dietrich Leibfried, David J. Wineland

Large-scale quantum information processors must be able to transport and maintain quantum information and repeatedly perform logical operations. Here, we show a combination of all of the fundamental elements required to perform scalable quantum computing through the use of qubits stored in the internal states of trapped atomic ions. We quantified the repeatability of a multiple-qubit operation and observed no loss of performance despite qubit transport over macroscopic distances. Key to these results is the use of different pairs of ^{9}Be$^+$ hyperfine states for robust qubit storage, readout, and gates, and simultaneous trapping of ^{24}Mg$^+$ "re-cooling" ions along with the qubit ions.
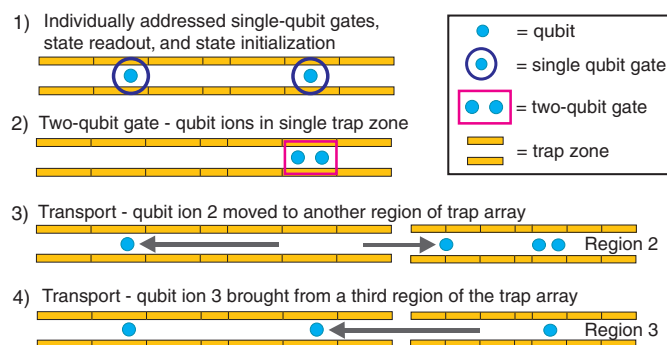
The long-term goal for experimental quantum information processing is to realize a device that involves large numbers of qubits and even larger numbers of logical operations (*1*, *2*). These resource requirements are defined both by the algorithms themselves and the need for quantum error correction, which makes use of many physical systems to store each qubit (*1*, *3*). The required components for building such a device are robust qubit storage, single- and two-qubit logic gates, state initialization, readout, and the ability to transfer quantum information between spatially separated locations in the processor (*2*, *4*, *5*). All of these components must be able to be performed repeatedly in order to realize a large-scale device.

One experimental implementation of quantum information processing uses qubits stored in the internal states of trapped atomic ions. A universal set of quantum logic gates has been demonstrated using laser addressing (*6–8*), leading to a number of small-scale demonstrations of quantum information protocols, including teleportation, dense-coding, and a single round of quantum error correction (*6*). A major challenge for this implementation is now to integrate scalable techniques required for large-scale processing.

A possible architecture for a large-scale trapped-ion device involves moving quantum information around the processor by moving the ions themselves, in which the transport is controlled by time-varying potentials applied to electrodes in a multiple-zone trap array (*5*, *9*, *10*). The processor would consist of a large number of processing regions working in parallel, with other regions dedicated to qubit storage (memory). A general prescription for the required operations in a single processing region is the following (Fig. 1), which includes all of the elements necessary for universal quantum computation (*11*): (i) Two qubit ions are held in separate zones, allowing individual addressing for single-qubit gates, state readout, or state initialization. (ii) The ions are then combined in a single zone, and a two-qubit gate is performed. (iii) The ions are separated, and one is moved to another region of the trap array. (iv) A third ion is brought into this processing region from another part of the device. In this work, we

Time and Frequency Division, National Institute of Standards and Technology (NIST), Boulder, CO 80305, USA.

*To whom correspondence should be addressed. E-mail: jonathan.home@gmail.com

Fig. 1. Schematic of the sequence of operations implemented in a single processing region for building up a computation in the architecture of (*5*, *9*). A large-scale device would involve many of these processing regions performing operations in parallel along with additional regions for memory. Generalized operations would use this block structure repeatedly, with perhaps some of the steps omitted.

1) Individually addressed single-qubit gates, state readout, and state initialization

2) Two-qubit gate - qubit ions in single trap zone

3) Transport - qubit ion 2 moved to another region of trap array — Region 2

4) Transport - qubit ion 3 brought from a third region of the trap array — Region 3

- ● = qubit
- ⊚ = single qubit gate
- ●● = two-qubit gate
- ▬ = trap zone

implemented in a repeated fashion all of the steps that must be performed in a single processing region in order to realize this architecture.

Some elements of this architecture have been demonstrated in previous experiments (*6, 12*), which involved transport of ions in a multiple-zone trap. However, these experiments did not involve the use of techniques required for building a large-scale device, limiting the size of algorithms that could be performed. Primary limiting factors for these experiments were the loss of qubit coherence, caused by interaction with the fluctuating magnetic field environment, and motional excitation, which degrades the fidelity of subsequent two-qubit gates because of the finite

wavelength of the gate control fields (*13*). Motional excitation occurs as a result of imperfect control during transport and noisy electric fields emanating from the electrode surfaces (*6*). In this work, we robustly stored qubits using a pair of energy eigenstates in the $^9Be^+$ 2s $^2S_{1/2}$ hyperfine manifold (Fig. 2), whose energy separation does not depend on the magnetic field to first order. For the $^9Be^+$ "qubit" ions used here, this condition is met at a magnetic field of 0.011964 T for the "memory" qubit states $|1\rangle \equiv |F = 1, M_F = 0\rangle$ and $|0\rangle \equiv |F = 2, M_F = 1\rangle$ (the states are labeled by using the total angular momentum quantum numbers F and M_F). The insensitivity to magnetic-field changes is crucial for preserving coherence in the

presence of ambient temporal field fluctuations (*14*) and also greatly suppresses phase shifts caused by spatial variations in the average field experienced by an ion as it is transported throughout the multiple-zone trap array. We removed motional excitation before each two-qubit gate by recooling "refrigerant" $^{24}Mg^+$ ions that were trapped along with the qubit ions. Laser-cooling this second species sympathetically cools the first through the strong Coulomb interaction between the ions (*15–18*).

A benchmark for scalability in this implementation is the repeated performance of a complete set of one- and two-qubit logic gates combined with quantum information transport. We demonstrated repeatability of a unitary transformation $\hat{U}$, which involves four single-qubit gates, a two-qubit gate, and transport over 960 μm (the sequence for $\hat{U}$ is shown in Fig. 3A). Ideally, $\hat{U}$ implements the operation

$$\hat{U} = -\frac{e^{-i\pi/4}}{\sqrt{2}}\begin{pmatrix} -1 & 0 & 0 & i \\ 0 & 1 & i & 0 \\ 0 & i & 1 & 0 \\ i & 0 & 0 & -1 \end{pmatrix} \quad (1)$$

Fig. 2. Hybrid qubit storage in the $^9Be^+$ 2s $^2S_{1/2}$ hyperfine levels. The states are labeled with the total angular momentum quantum numbers F and M_F. $|1\rangle$, $|0\rangle$ are the qubit states used for single-qubit gates and transport, and $|1_G\rangle$, $|0_G\rangle$ are used for two-qubit gates. For detection, the $|1,-1\rangle$ and $|2,2\rangle$ states are used. At the applied magnetic field ($B \cong 0.011964$ T), the frequencies for transitions between pairs of states with the same F are well resolved.

$|F=1, M_F=-1\rangle$ $|1,0\rangle \equiv |1\rangle$ $|1,1\rangle \equiv |1_G\rangle$

$|2,-2\rangle$ $|2,-1\rangle$ $|2,0\rangle$ $|2,1\rangle \equiv |0\rangle$ $|2,2\rangle \equiv |0_G\rangle$

in the $|11\rangle, |10\rangle, |01\rangle, |00\rangle$ basis. We directly compared experimental implementation of $\hat{U}$ and $\hat{U}^2$ using quantum process tomography (*19*). Process tomography requires the process under investigation to be applied to 16 input states followed by measurement in nine orthogonal bases (*20*). The input states were prepared by use of a combination of optical pumping and single-qubit operations, with the latter performed on each qubit individually. The analysis also requires individual single-qubit rotations followed by individual state-measurement of the qubits. The experiment therefore realizes all of the basic components illustrated in Fig. 1. We directly compared $\hat{U}$ and $\hat{U}^2$ by running the experimental sequence for a given input/output combination on $\hat{U}$ and $\hat{U}^2$ sequentially (Fig. 3B), making the comparison of the two

Fig. 3. (**A**) Schematic of the qubit ion trajectories (the solid red line indicates qubit 1 and the dotted blue line indicates qubit 2) and gate operations used to implement $\hat{U}$. The single-qubit rotations are $\pi/2 \equiv R(\pi/2, 0)$ (Eq. 2). The two-qubit gate implements $\hat{G} = D[(1,i,i,1)]$. (**B**) Full sequence used to perform process tomography on $\hat{U}$ and $\hat{U}^2$. This sequence was repeated 350 times for each setting of preparation/analysis.
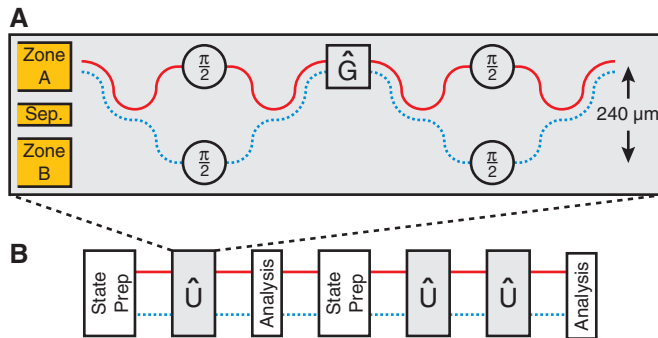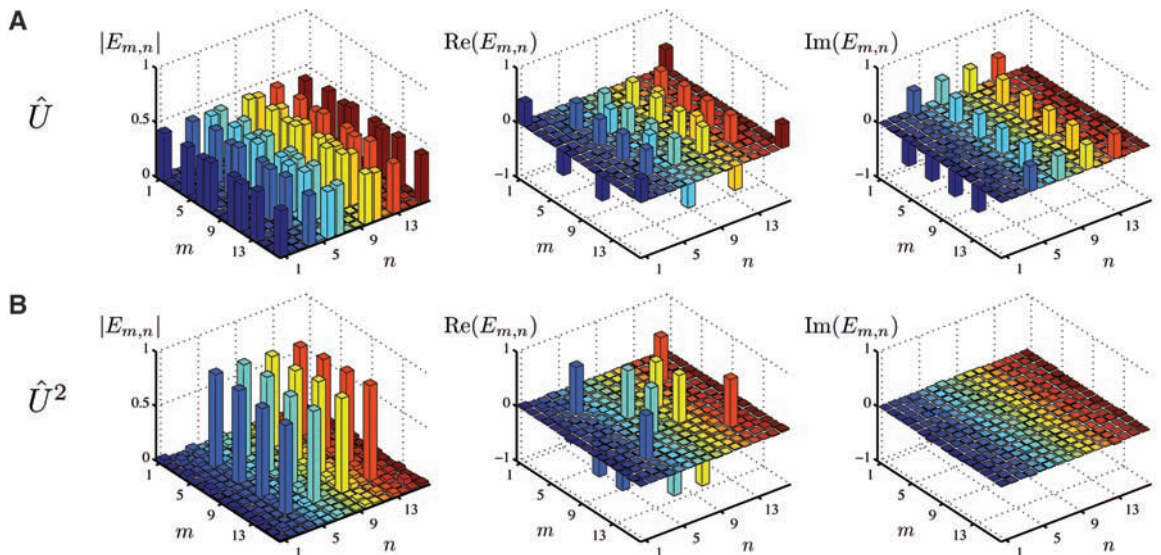
Fig. 4. Reconstructed process matrix for (**A**) $\hat{U}$ and (**B**) two repetitions of $\hat{U}$. The map $\mathcal{E}(|i\rangle\langle j|)$ produces a matrix $\mathcal{E}_{kl}$ for each element $|i\rangle\langle j|$. Hence, elements of the matrix E are labeled by $m = 4(i-1) + k$, $n = 4(j-1) + l$, where the factor 4 results from the size of the two-qubit state space. For example, the $|11\rangle\langle00|$ ($i = 1, j = 4$) element of an input density matrix is mapped to $\mathcal{E}(|11\rangle\langle00|)$, a 4 by 4 block of E given by $m \in [1, 4]$ and $n \in [13, 16]$. The position of each peak is in agreement with the theoretical prediction.

robust against long-term drifts in experimental parameters. For each input/analysis combination, we repeated this sequence 350 times.

The experiment used two ^{9}Be$^+$ and two ^{24}Mg$^+$ ions trapped in a six-zone linear Paul trap (12). Each ^{9}Be$^+$ ion was used to store one qubit and was accompanied at all times by a ^{24}Mg$^+$ refrigerant ion, which was used for sympathetic cooling. The ion order was initialized to ^{9}Be$^+$–^{24}Mg$^+$–^{24}Mg$^+$–^{9}Be$^+$ at the start of the experimental sequence and remained in this order throughout (21).

We performed coherent manipulations of the internal and motional states of the ions using laser-induced stimulated Raman transitions (9). Single-qubit gates were implemented in the basis $|1\rangle$, $|0\rangle$ by means of resonant Rabi flopping, applying the rotation

$$
\begin{aligned}
&R(\theta, \phi) \\
&= \begin{pmatrix} \cos(\theta/2) & -ie^{-i\phi}\sin(\theta/2) \\ -ie^{i\phi}\sin(\theta/2) & \cos(\theta/2) \end{pmatrix}
\end{aligned}
\tag{2}
$$

where θ is proportional to the Raman pulse duration and ϕ was chosen by adjusting the relative phase of the Raman light fields at the ion. We individually addressed the two-qubit ions by holding them in two trap zones 240 μm apart and switching the laser beams between zones.

To implement two-qubit gates, we first combined all of the ions into a single zone. The four-ion linear chain exhibits four axial vibrational normal modes caused by the Coulomb coupling between ions (21). After recombination, these modes contain significant excess energy, which is mainly caused by imperfect control of the potentials used during separation and recombination. Therefore, before each two-qubit gate we cooled each mode to near the quantum ground state ($\langle n \rangle \sim 0.06$) using a combination of Doppler cooling and resolved sideband cooling on the ^{24}Mg$^+$ ions (15, 22). The cooling light only interacts with ^{24}Mg$^+$, leaving the qubits stored in ^{9}Be$^+$ intact (15).

The composite two-qubit gate makes use of a geometric phase gate (7) to implement $\hat{G} = D[(1, i, i, 1)]$, where $D[\underline{v}]$ is a diagonal matrix with the vector $\underline{v}$ on the diagonal. The phase acquired by the $|10\rangle$ and $|01\rangle$ states was obtained by means of transient simultaneous excitation of the two highest-frequency normal modes by use of a state-dependent optical dipole force (22). The state dependence of this force is derived from a differential light shift between the two-qubit states, which is highly suppressed for field-independent transitions (14, 23). We thus used a hybrid scheme for qubit storage, mapping the qubits into a different state manifold for the two-qubit gate (22, 24, 25). Before applying the optical dipole force, we transferred each qubit into a pair of states with a sizeable differential light shift—the "gate" manifold $|1_G\rangle \equiv |1,1\rangle$, $|0_G\rangle \equiv |2,2\rangle$ (Fig. 2). After applying the state-dependent force, we reversed this transfer and the ions were again separated (22). The gate manifold is sensitive to

magnetic-field fluctuations, which can lead to qubit dephasing. We suppressed these effects using spin-echo techniques (21).

We used quantum process tomography to characterize our implementation of the unitary operation $\hat{U}$, including any experimental imperfections (19, 20). The evolution of the qubit system (including that caused by undesired interactions with the environment) is described by a completely positive linear map $\rho_{\text{out}} = \mathcal{E}_{\hat{U}}(\rho_{\text{in}})$ (19) on the input density matrix $\rho_{\text{in}} = \sum_{i,j} c_{i,j} |i\rangle \langle j|$, where the $c_{i,j}$ are complex numbers and i, j are labels that each run over the eigenstates $|11\rangle$, $|10\rangle$, $|01\rangle$, and $|00\rangle$. Following the method described in (26), we represent the map with a 16 by 16 matrix

$$
E_{\hat{U}} = \sum_{i,j} |i\rangle \langle j| \otimes \mathcal{E}_{\hat{U}}(|i\rangle \langle j|)
\tag{3}
$$

In order to extract this process matrix, we experimentally applied the process to 16 input states made up of tensor products of the states $|1\rangle$, $|0\rangle$, $(|0\rangle - |1\rangle)/\sqrt{2}$, and $(|0\rangle + i|1\rangle)/\sqrt{2}$. For each output-density matrix, we applied nine sets of rotations, which allowed us to measure the expectation values of the operators $\sigma_s \otimes \sigma_t$, where the $\sigma_{s,t}$ run over the Pauli matrices I, σ_x, σ_y, and σ_z. Our state readout performs a projective measurement in the Z basis on each ion independently. We first transferred population from $|0\rangle$ to $|2,2\rangle$, and from $|1\rangle$ to $|1,-1\rangle$ and subsequently drove the cycling transition 2s ^{2}S$_{1/2}$ $|2,2\rangle \leftrightarrow$ 2p ^{2}P$_{3/2}$ $|3,3\rangle$ for 200 μs, in which $|2,2\rangle$ strongly fluoresces and $|1,-1\rangle$ does not (22). We collected a small fraction of the emitted photons on a photomultiplier tube. We ran the sequence shown in Fig. 3B 350 times for each of the 16 input states and nine measurement rotations. The process matrix was obtained directly from the recorded photon counts and measurement/preparation settings by means of a maximum-likelihood method that ensures that the reconstructed process matrix is physical (26).

Experimentally obtained process matrices for one and two applications of $\hat{U}$ are shown in Fig. 4. From the reconstructions, we can calculate various measures of the fidelity with which the processes were implemented. A direct comparison between experimental results and the ideal case is given by the entanglement fidelity $F \equiv \text{Tr}(E_{\text{ideal}} E)/16$ (27). We found $F_{\hat{U}} = 0.922(4)$ for a single application of $\hat{U}$ and $F_{\hat{U}^2} = 0.853(5)$ for two applications [error estimates are the SE on the mean obtained from parametric bootstrap resampling (22)]. As an additional measure of operation fidelity, we took the mean $\overline{f}$ of the fidelity $f(\rho_{\text{ideal}}, \rho_E) \equiv [\text{Tr}(\sqrt{\sqrt{\rho_{\text{ideal}}} \rho_E \sqrt{\rho_{\text{ideal}}}})]^2$ (28) between the output-density matrices obtained from the ideal and experimental processes for an unbiased set of 36 input states (formed from the eigenstates of $\sigma_s \otimes \sigma_t$, where $\sigma_{s,t}$ run over σ_x, σ_y, and σ_z). We obtained a mean state fidelity of $\overline{f}_{\hat{U}} = 0.940(4)$ for $E_{\hat{U}}$ and $\overline{f}_{\hat{U}^2} = 0.890(4)$ for $E_{\hat{U}^2}$. We can compare these values with the entanglement fidelities by using the relation $\overline{f} = (4F+1)/5$ (27) and see that they are consistent.

To compare the performance of a second application of $\hat{U}$ relative to the first, we can compare its experimental repetition $\mathcal{E}_{\hat{U}^2}(\rho_{\text{in}})$ to a numeric repetition of the experimental map $\mathcal{E}_{\hat{U}}(\rho_{\text{in}})$; that is, to $\mathcal{E}_{\hat{U}\hat{U}}(\rho_{\text{in}}) \equiv \mathcal{E}_{\hat{U}}[\mathcal{E}_{\hat{U}}(\rho_{\text{in}})]$. Evaluating the fidelities for each against the ideal case yields $F_{\hat{U}^2}/F_{\hat{U}\hat{U}} = 1.003(13)$ and $\overline{f}_{\hat{U}^2}/\overline{f}_{\hat{U}\hat{U}} = 1.004(10)$, indicating that the operation fidelity is the same for each application of $\hat{U}$. We can also make a direct comparison between the processes performed by our implementation of $\hat{U}$ and $\hat{U}^2$ by taking the mean fidelity between $\rho_{\hat{U}\hat{U}} = \mathcal{E}_{\hat{U}}[\mathcal{E}_{\hat{U}}(\rho_{\text{in}})]$ and $\rho_{\hat{U}^2} = \mathcal{E}_{\hat{U}^2}(\rho_{\text{in}})$ for the 36 input states. We find $\overline{f}(\rho_{\hat{U}\hat{U}}, \rho_{\hat{U}^2}) = 0.987(3)$. Although this number is not unity, as might be expected, the deviation can be ascribed to bias in the maximum-likelihood reconstruction method for a finite sample size (22). Our results are thus consistent with the same operation being performed by the experiment for each application of $\hat{U}$.

Sources of error in our system arise primarily from spontaneous photon scattering ($\sim 1.5\%$ per $\hat{U}$) (29) and intensity fluctuations of the Raman light fields at the percent level. In order to characterize the loss of fidelity caused by single-qubit rotations, we applied process tomography to the experimental sequence but without the state-dependent force pulses. In this case, the ions are always in a product state, and the process matrix for each can be obtained independently. The resulting process matrices have a mean state fidelity relative to the ideal case of 0.97 for a single run of the sequence (which uses eight rotations per ion, including qubit-manifold transfer and spin-echo pulses). During the two-qubit gate, the spin states are entangled with the motion. From separate measurements of motional coherence, we estimate the infidelity from this source to be less than 1×10^{-3}.

Many challenges remain before large-scale ion trap quantum information processing becomes a reality, including increasing fidelities to those required for fault-tolerant quantum error correction (1, 3) and meeting the considerable technical challenge of controlling ions in large multidimensional trap arrays (10). Both of these challenges could potentially contain problems that have not been considered here and may require combining our approach with alternative methods, for instance entanglement distribution by means of photonic networks (30). Nevertheless, the combination of techniques demonstrated here includes all of the basic building blocks required in this architecture and opens up new possibilities for quantum information processing as well as state and process engineering.

References and Notes
1. E. Knill, *Nature* **434**, 39 (2005).
2. A. M. Steane, *Quant. Inf. Comp.* **7**, 171 (2007).
3. A. M. Steane, *Phys. Rev. A* **68**, 042322 (2003).
4. D. P. DiVincenzo, *Fortschr. Phys.* **48**, 771 (2000).
5. D. Kielpinski, C. Monroe, D. J. Wineland, *Nature* **417**, 709 (2002).
6. R. Blatt, D. J. Wineland, *Nature* **453**, 1008 (2008).
7. D. Leibfried *et al.*, *Nature* **422**, 412 (2003).

1229

8. J. Benhelm, G. Kirchmair, C. F. Roos, R. Blatt, *Nat. Phys.* **4**, 463 (2008).
9. D. J. Wineland *et al.*, *J. Res. Natl. Inst. Stand. Technol.* **103**, 259 (1998).
10. R. B. Blakestad *et al.*, *Phys. Rev. Lett.* **102**, 153002 (2009).
11. A. Barenco *et al.*, *Phys. Rev. A* **52**, 3457 (1995).
12. M. D. Barrett *et al.*, *Nature* **429**, 737 (2004).
13. A. Sørensen, K. Mølmer, *Phys. Rev. A* **62**, 022311 (2000).
14. C. Langer *et al.*, *Phys. Rev. Lett.* **95**, 060502 (2005).
15. M. D. Barrett *et al.*, *Phys. Rev. A* **68**, 042302 (2003).
16. H. Rohde *et al.*, *J. Opt. B Quantum Semiclass. Opt.* **3**, S34 (2001).
17. B. B. Blinov *et al.*, *Phys. Rev. A* **65**, 040304 (2002).
18. J. P. Home *et al.*, *Phys. Rev. A* **79**, 050305 (2009).
19. M. A. Nielsen, I. L. Chuang, *Quantum Computation and Quantum Information* (Cambridge Univ. Press, Cambridge, 2000).
20. M. Riebe *et al.*, *Phys. Rev. Lett.* **97**, 220407 (2006).
21. J. D. Jost *et al.*, *Nature* **459**, 683 (2009).
22. Material and methods are available as supporting material on *Science* Online.
23. P. J. Lee *et al.*, *J. Opt. B Quantum Semiclass. Opt.* **7**, S371 (2005).
24. N. Lundblad, J. M. Obrecht, I. B. Spielman, J. V. Porto, *arXiv:0902.3213* (2009).
25. G. Kirchmair *et al.*, *Phys. Rev. A* **79**, 020304 (2009).
26. Z. Hradil, J. Řeháček, J. Fiurášek, M. Ježek, *Quantum State Estimation* (Springer-Verlag, 2004), pp. 59–112.
27. M. Horodecki, P. Horodecki, R. Horodecki, *Phys. Rev. A* **60**, 1888 (1999).
28. R. Jozsa, *J. Mod. Opt.* **41**, 2315 (1994).
29. R. Ozeri *et al.*, *Phys. Rev. A* **75**, 042329 (2007).
30. D. L. Moehring *et al.*, *Nature* **449**, 68 (2007).

A Sulfilimine Bond Identified in Collagen IV

Roberto Vanacore,[1]* Amy-Joan L. Ham,[2]† Markus Voehler,[3] Charles R. Sanders,[2] Thomas P. Conrads,[5]‡ Timothy D. Veenstra,[5] K. Barry Sharpless,[6] Philip E. Dawson,[6,7] Billy G. Hudson[1,2,4]*

Collagen IV networks are ancient proteins of basement membranes that underlie epithelia in metazoa from sponge to human. The networks provide structural integrity to tissues and serve as ligands for integrin cell-surface receptors. They are assembled by oligomerization of triple-helical protomers and are covalently crosslinked, a key reinforcement that stabilizes networks. We used Fourier-transform ion cyclotron resonance mass spectrometry and nuclear magnetic resonance spectroscopy to show that a sulfilimine bond (-S=N-) crosslinks hydroxylysine-211 and methionine-93 of adjoining protomers, a bond not previously found in biomolecules. This bond, the nitrogen analog of a sulfoxide, appears to have arisen at the divergence of sponge and cnidaria, an adaptation of the extracellular matrix in response to mechanical stress in metazoan evolution.

Collagen IV networks are ancient proteins of basement membranes, a specialized form of extracellular matrix, that underlie epithelia in metazoa from sponge to human. The networks confer structural integrity to tissues; serve as scaffolds for the assembly of other macromolecular components; and serve as ligands for integrin cell-surface receptors that mediate cell adhesion, migration, growth, and differentiation (*1–3*). The networks participate in signaling events in *Drosophila* development (*4*) and in the clustering of receptors in the development of mammalian neuromuscular junction (*5*), and they are involved in autoimmune and genetic diseases (*6–8*). The networks are assembled by oligomerization of triple-helical protomers by end-to-end associations and by intertwining of triple helices (*9*, *10*). At the C terminus, two protomers associate through their trimeric noncollagenous (NC1) domains, forming a hexamer structure. The protomer-protomer interface is covalently crosslinked, a key reinforcement that strengthens the structural integrity of networks. In the case of humans, the crosslink also confers immune privilege to the collagen IV antigen of Goodpasture autoimmune disease (*11*, *12*).

The chemical nature of these crosslinks has been the subject of numerous investigations for

2 decades; yet, the identity of the covalent bond has remained unknown. Initially, the crosslinks were identified as disulfide bonds (*13*), which were subsequently ruled out by the x-ray crystal structure of NC1 hexamers (*14*, *15*). Electron density maps suggested connectivity between methionine-93 (Met^{93}) and lysine-211 (Lys^{211}) at the interface of adjoining protomers (*15*); however, the connectivity is gradually degraded by x-rays, rendering precise characterization a challenge for structural analysis by crystallography (*16*, *17*). By using mass spectrometry (MS) analyses of crosslinked tryptic (Tp) peptides and smaller crosslinked post-proline endopeptidase (PPE) peptides, both derived from the α1α2α1 collagen IV network of placenta, we found that Lys^{211} is modified to hydroxylysine (Hyl^{211}) and that Hyl^{211} is covalently linked to Met^{93}, forming a *S*-hydroxylysyl-methionine (sHM) crosslink (*18*). In the α3α4α5 network (*11*), we found that the sHM crosslink connects the α3 and α5 NC1 domains but that the α4 NC1 domains are connected by a *S*-lysyl-methionine crosslink involving Lys^{211} instead of Hyl^{211}, indicating that this posttranslational modification is not a requirement for crosslink formation (*11*). The nature of the bond linking Met^{93} and Hyl^{211} could not be determined at that time because the observed difference of one mass unit between the uncrosslinked and crosslinked peptides fell within experimental error.

Herein, we deduce the chemical nature of the bond by using Fourier transform ion cyclotron resonance (FTICR) MS (*19*), which can achieve very high mass accuracy [e.g., < 2 parts per million (ppm), about ±0.001 mass units for a peptide with a mass of ~5000], and nuclear magnetic resonance (NMR) spectroscopy to

[1]Division of Nephrology, Department of Medicine and Center for Matrix Biology, Vanderbilt University, Nashville, TN 37232, USA. [2]Department of Biochemistry, Vanderbilt University, Nashville, TN 37232, USA. [3]Department of Chemistry, Vanderbilt University, Nashville, TN 37232, USA. [4]Department of Pathology, Vanderbilt University, Nashville, TN 37232, USA. [5]Laboratory of Proteomics and Analytical Technologies, Advanced Technology Program, SAIC-Frederick, Incorporated, National Cancer Institute, Frederick, MD 21702, USA. [6]Department of Chemistry and The Skaggs Institute for Chemical Biology, The Scripps Research Institute, La Jolla, CA 92037, USA. [7]Department of Cell Biology, The Scripps Research Institute, La Jolla, CA 92037, USA.

*To whom correspondence should be addressed. E-mail: roberto.vanacore@vanderbilt.edu (R.V.); billy.hudson@vanderbilt.edu (B.G.H.)
†Present address: Jim Ayers Institute for Precancer Detection and Diagnosis, Vanderbilt University School of Medicine, Nashville, TN 37232, USA.
‡Present address: Department of Pharmacology, University of Pittsburgh School of Medicine, Pittsburgh, PA 15213, USA.

Table 1. Mass values for the crosslinked Tp peptides from the α1NC1-α1NC1 dimer. The average of the observed peptide mass is indicated with an asterisk.

Z	Theoretical mass	Observed ion (*m/z*)	Observed peptide mass	Difference (theo. − obs.)
+4		1253.6204	5010.473 ± 0.008	
+5		1003.1014	5010.483 ± 0.022	
+6		836.0806	5010.459 ± 0.009	
	5012.488		5010.471 ± 0.022*	2.017